The following publication Zhu, T., Liu, S., Huang, B., Shao, Q., Wang, M., Li, F., ... & Huang, X. (2021). High-performance diluted nickel nanoclusters decorating ruthenium nanowires for pH-universal overall water splitting. Energy & Environmental Science, 14(5), 3194-3202 is available at https://doi.org/10.1039/d0ee04028b.

High-Performance Diluted Nanoclusters-Activated Ruthenium Nanowires for pH-Universal Overall Water Splitting

Ting Zhu[a,b#], Shangheng Liu[a#], Bin Huang[b#], Qi Shao[a,c*], Fan Li[d], Xinyue Tan[a], Yecan Pi[a], Shih-Chang Weng[e], Bolong Huang[f*], Zhiwei Hu[g], Jianbo Wu[d], Yong Qian[b], and Xiaoqing Huang[a,h*]

Developing a versatile electrocatalyst with remarkable performance viable for pH-universal overall water splitting is increasingly important for the industrial production of renewable energy conversion. Herein, our theoretical calculations predicate that the limitations in the mean-field behavior from the traditional catalyst designing strategy can be largely overcome by introducing diluted metal nanoclusters, which can lead to optimal thermodynamic effect for enhancing electron-transfer capability, and in turn promote the activation of initial water-dissociation for both hydrogen evolution reaction and oxygen evolution reaction. As a proof of concept, a unique catalyst, namely diluted nickel nanoclusters-decorated ruthenium nanowires, was explored as a high-performance electrocatalyst for overall water splitting. The optimized catalyst delivered record activity for overall water splitting in a wide pH range from 0 to 14 with all the potentials lower than 1.454 V to achieve the current density of 10 mA cm^{-2}, largely outperforming the Pt/C-Ir/C integrated couple. It also readily reaches a high current density, of up to 100 mA cm^{-2}, with a low voltage of only 1.55 V applied. It is further demonstrated that the diluted nickel nanoclusters can strongly anchor on the ruthenium nanowires, contributing to the enhanced stability after the long-term tests. The diluted metal nanoclusters-activated strategy highlights a general pathway for the rational design of catalysts with unprecedented performance for electrocatalysis and beyond.

Introduction

With dwindling supplies of fossil fuels and their adverse effects on the environment, considerable emphasis has been placed on developing clean renewable energy sources.[1-3] Electrochemical water splitting provides an effective pathway to address the growing energy crisis by producing high-purity hydrogen (H_2) in high efficiency, low cost and sustainability fashion.[4-6] However, current electrocatalysts still require large cell voltages to drive water splitting due to their unfavourable reaction kinetics.[7, 8] Another grand challenge also remains about the limited catalysts those applicable for pH-universal conditions, which severely hampers the practical applications of water splitting.[9-11] These critical issues prompt seeking alternative means to develop exceptionally efficient catalysts that enable high-performance pH-universal overall water splitting.

For a given reaction, engineering the local electronic structure of catalysts tailors its catalytic performance.[12] However, the previous catalysts often exhibit a mean-field dominated behaviour for their broad electronic band structures, resulting in the restrictions upon realizing the fine-control of chemical bonding strength, thermodynamic optimization and achievable catalytic performance.[13, 14] In order to achieve exceptional catalytic behaviour, reconstructing the surface of the catalyst by introducing a performed component with unusual electronic structure, and thus fulfilling the optimized control between active sites and intermediates is highly required.[15, 16]

Herein, we chose ruthenium (Ru) as the matrix metal for catalyst design due to its potential performances for half-reactions (hydrogen evolution reaction (HER) and oxygen evolution reaction (OER)).[11] Taking advantage of the theoretical calculation, it reveals that introducing diluted metal nanoclusters into matrix metals give rise to the optimization of thermodynamic value for its powerful effect on precisely narrowing the band states. Such modification largely increases the possibilities of fulfilling the optimized control between active sites and intermediates. We are further motivated to construct a model catalyst: diluted nickel nanoclusters-decorated ruthenium nanowires ($Ni_{cluster}$-Ru NWs). The Ru surface not only illustrates the pinning effect on the Ni-3*d* bands but also displays the good electronic conductivity for boosting up the

---

[a] *College of Chemistry, Chemical Engineering and Materials Science, Soochow University, Jiangsu 215123, P. R. China.*
[b] *Jiangxi Province Key Laboratory of Polymer Micro/Nano Manufacturing and Devices, East China University of Technology, Nanchang, Jiangxi 330013, P. R. China.*
[c] *Guangdong Provincial Key Laboratory of Energy Materials for Electric Power, Southern University of Science and Technology, Shenzhen 518055, P. R. China.*
[d] *School of Materials Science and Engineering, Shanghai Jiao Tong University, Shanghai, 200240, P. R. China.*
[e] *National Synchrotron Radiation Research Center, Hsinchu, 30076, Taiwan.*
[f] *Department of Applied Biology and Chemical Technology, The Hong Kong Polytechnic University, Hung Hom, Kowloon, Hong Kong SAR.*
[g] *Max-Planck-Institute for Chemical Physics of Solids, Nöthnitzer Street, 4001187, Dresden, Germany.*
[h] *College of Chemistry and Chemical Engineering, Xiamen University, Xiamen, 361005, P. R. China.*
[#] These authors contributed equally to this work.
Electronic Supplementary Information (ESI) available: [details of any supplementary information available should be included here]. See DOI: 10.1039/x0xx00000x
E-mail: bhuang@polyu.edu.hk; hxq006@xmu.edu.cn; qshao@suda.edu.cn

electron transfer during HER and OER. The optimized catalyst enables superior performance for overall water splitting with delivering the potentials lower than 1.454 V to achieve the current density of 10 mA cm^{-2} in the pH-universal condition, much lower than those of the commercial Pt/C and Ir/C. Detailed characterizations also reveal the effective and strong stabilization of diluted Ni nanoclusters on Ru nanowires after long-term stability test, promoting its further commercial application.

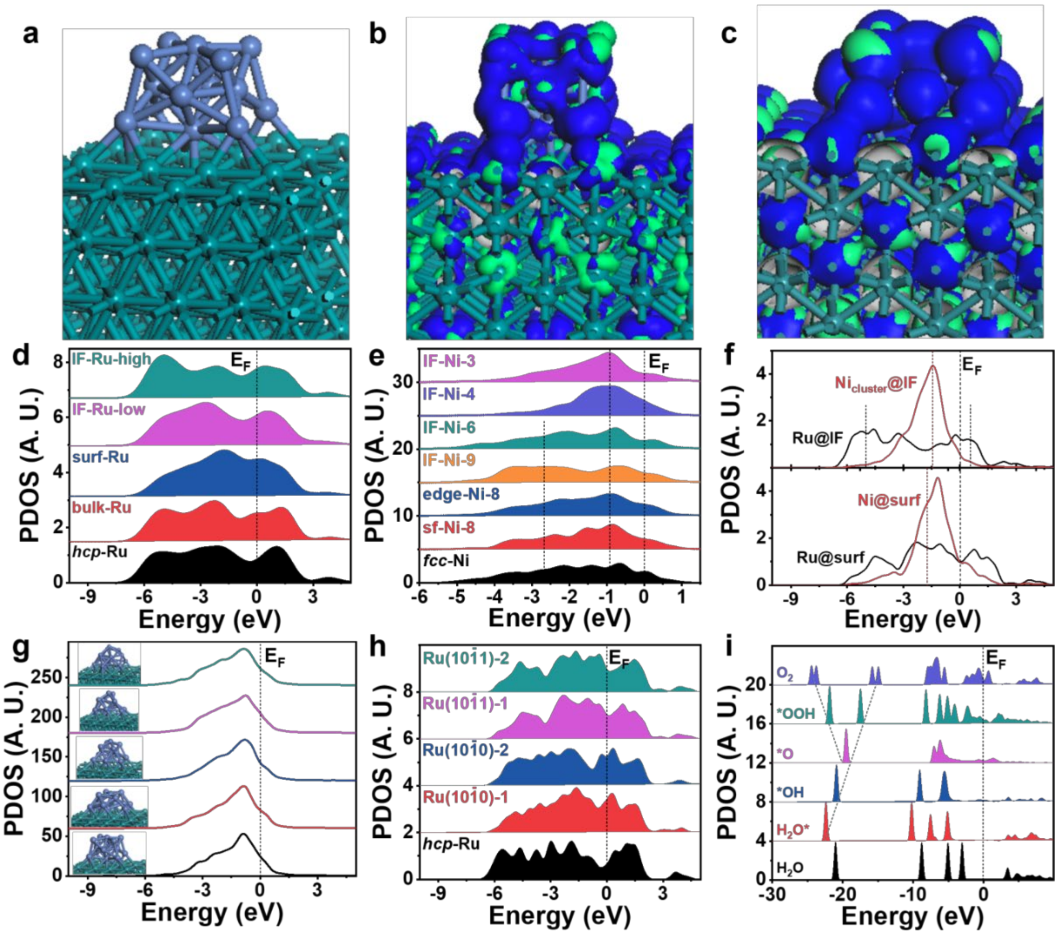

Fig. 1 Theoretically interpreted electronic activities for HER and OER. (a) Structural configurations of Ni$_{cluster}$-Ru. (b-c) The real spatial 3D orbital contour plots of Ru surfaces with different Ni cluster structures. The blue color represents the bonding orbitals while the green colors represent the anti-bonding orbitals. (d) The site-dependent PDOSs of Ru-4*d* band from the surface to the bulk states. IF is the interface region between Ni cluster and Ru NWs. Surf is the surface region of Ru NWs. IF-Ru-high and low represent the Ru sites with high and low coordinated numbers at the interface with the Ni cluster. (e) The site-dependent PDOSs of the Ni-3*d* band within the cluster. The number represents the coordination numbers of the Ni site at the interface region with Ru nanowires. The edge-Ni-8 and sf-Ni-8 represent the Ni sites with a coordination number of 8 at the edge and surface of the Ni cluster, respectively. (f) The PDOSs comparison of Ru-4*d* and Ni-3*d* bands at the interface and surface. (g) The PDOSs of Ni-3*d* bands within different clusters on the Ru surface. Five models show different structural configurations of Ni cluster. (h) The PDOSs comparison Ru on different surfaces and bulk states. Ru(10-10)-1 and Ru(10-11)-1 represent the larger size Ni clusters on different surfaces of Ru NWs. Ru(10-10)-2 and Ru(10-11)-2 represent the smaller size Ni clusters on different surfaces of Ru NWs. (i) PDOSs of O-2*p* bands of O-intermediates during the OER process.Structure characterizations of Cu/Pb core/shell NCs. (a) Atomic profile model of Cu/Pb core/shell electrocatalysts. (b) HAADF-STEM image, (c) EDS elemental mapping images, (d) HRTEM image and (e) the magnified HRTEM image in (d) of CuPb-0.7 NCs. (f) HRTEM image and (g) the magnified HRTEM image in (f) of CuPb-1.5 NCs. Scale bars, 1 nm in (f) and (g), 5 nm in (d) and (e), 20 nm in (b) and (c).

Results and discussion

To investigate the influence of the introduction of nanoclusters on modifying the electronic structure of Ru, we first conducted the theoretical study based on the density functional theory (DFT) calculations from the electronic perspective. The established model with anchoring Ni cluster on the Ru surface is shown in **Fig. 1a**. The comparison of the active bonding and anti-bonding orbitals near the Fermi level (E_F) are demonstrated. Even for different structural configurations of Ni cluster, the electron active regions (blue isosurface) is always identified on the Ni cluster, which loosens the forbidden *d-d* electron transfer between Ni and Ru sites. This optimized electronic environment improves the electron-transfer efficiency between electrocatalyst and the adsorbates (**Fig. 1b-c**). Then, we move to the detailed electronic investigation based on the projected partial density of states (PDOS). For the site-dependent PDOS of Ru, we notice that the electronic structure of bulk Ru has not been affected, which is similar to the metallic Ru. Meanwhile, after the introduction of the Ni cluster on the surface, it is noted that surface Ru-4*d* orbitals experience evident splitting at the interface, which indicates the modulation of electron structure by the anchoring of Ni cluster (**Fig. 1d**). For the Ni cluster on Ru, the surface Ni still preserves a similar electronic structure with *fcc*-Ni, displaying broadband covering from E_v-5.0 eV towards E_F ($E_V = 0$ for E_F). Within the cluster, for the Ni-sites closer to the interface with Ru NWs, Ni-3*d* becomes narrow with an evident sharp peak locating near E_v-0.9 eV, which play as the active sites for the adsorption of proton and *OH in both HER and OER. This 3*d*-band evolution of Ni at the interfaces arises from the isolation by the Ru-4*d* band. (**Fig. 1e**). To further examine the local electronic structures, the PDOS comparison of interface and surface has been illustrated. Notably, with the pinning effect of Ru-4*d* bands, the Ni-3*d* bands have been firmly pinned within the region of E_v-0.90 ~ E_v-1.10 eV in both surface and interface, which result in the stable electroactivity for the Ni site to boost up the electron transfer for water-splitting in both acidic and alkaline media (**Fig 1f**). The pinning of the Ni-3*d* band induced by the Ru-4*d* has also been verified in different cluster structures on the Ru surface. For Ni cluster with varied structural configurations, the surface electronic structures show the barely changed Ni-3*d* bands, supporting the key role of Ni cluster decoration for promoting the water-splitting performance. Meanwhile, the Ru-4d bands also alleviates the overbinding effect of Ni for the adsorption of proton and *OH (**Fig. 1g**). Moreover, when comparing the electronic structure of Ru NWs with different size of Ni cluster, the lowest index surface Ru (10-10) exhibits a high electron density near Fermi level, which supports a good electronic conductivity to guarantee the efficient electron transfer during the electrocatalysis. In comparison, the Ru (10-11) surfaces and bulk Ru shows much weaker electron transfer capability. In addition, the larger size of the Ni cluster on Ru NWs shows a more saturated electron density near E_F than the smaller size, supporting the significant role of Ni cluster in promoting the electron transfer (**Fig. 1h**). For the PDOSs of the H_2O adsorption and O-intermediate species, we have noticed the linear evolution trend of O-2*p* sigma-band has been well preserved along with the OER reaction coordinates. This confirms the efficient electron-transfer between surface Ru-4*d* and adsorbed intermediates (**Fig. 1i**).

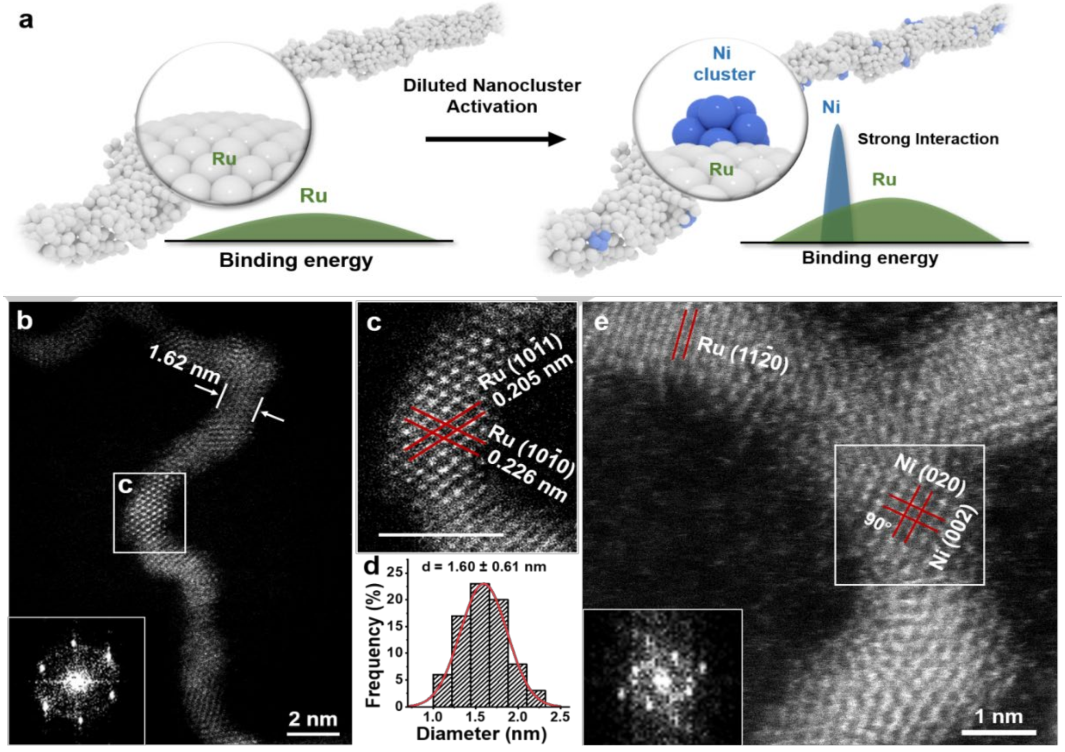

Fig. 2 Characterizations of $Ni_{cluster}$-Ru NWs. (a) The schematic illustration of the diluted metal nanoclusters-activated strategy. (b) Atomic resolution HAADF-STEM image (inset: FFT pattern of from the selected area), (c) HRTEM image from the selected area (scale bar: 2 nm). (d) Diameter histogram of $Ni_{cluster}$-Ru NWs. (e) High-resolution HAADF-STEM image of $Ni_{cluster}$-Ru NWs (inset: FFT pattern of from the selected area).

In light of these findings, we sought to construct a diluted nanoclusters-decorated metal system following the DFT calculation (**Fig. 2a**). As a primary attempt, the $Ni_{cluster}$-Ru NWs were successfully synthesized through a simple wet-chemical method, where K_2RuCl_5 and $Ni(HCOO)_2$ were chosen as metal precursors (**Fig. S1**). The morphology and structure of Ni$_{cluster}$-Ru NWs were first characterized by high-angle annular dark field scanning transmission electron microscopy (HAADF-STEM). The high yield of NWs with the average diameter of 1.60 nm was clearly observed. The energy-dispersive X-ray spectroscopy (EDS) spectrum indicated that the NWs contained mainly Ru and Ni with the atomic ratio determined of 94.0 : 6.0 (**Fig. S1f**). The powder X-ray diffraction (PXRD) pattern shows the broadened diffraction peaks, indicating the small diameter of Ni$_{cluster}$-Ru NWs and Ru NWs. Hardly peak shift is observed, suggesting that the Ni is not introduced into the Ru lattice (**Fig. S2**).[17]

The structure was further examined by atomic resolution aberration-corrected HAADF-STEM. As shown in **Fig. 2b**, Ni$_{cluster}$-Ru NWs exhibit the lattice fringes of 0.205 nm and 0.226 nm, which can be assigned to the (10-11) and (10-10) planes of Ru (**Fig. 2c**). The diameter is very small (~1.6 nm) (**Fig. 2d**). The magnified STEM image is uesd to reconfirm the existence of Ni nanocluster on the Ru nanowires. As shown in the modified **Fig. 2e**, the lattice spaces of (002) and (020) are clearly observed with the angel of 90°, indicating the existence of the Ni cluster. The inset electron diffraction pattern also matches well with Ni. Moreover, the nanometre-sized bright protrusions, further revealing that the Ni nanoclusters are sparsely supported on Ru nanowires (**Fig. S3**).[18]

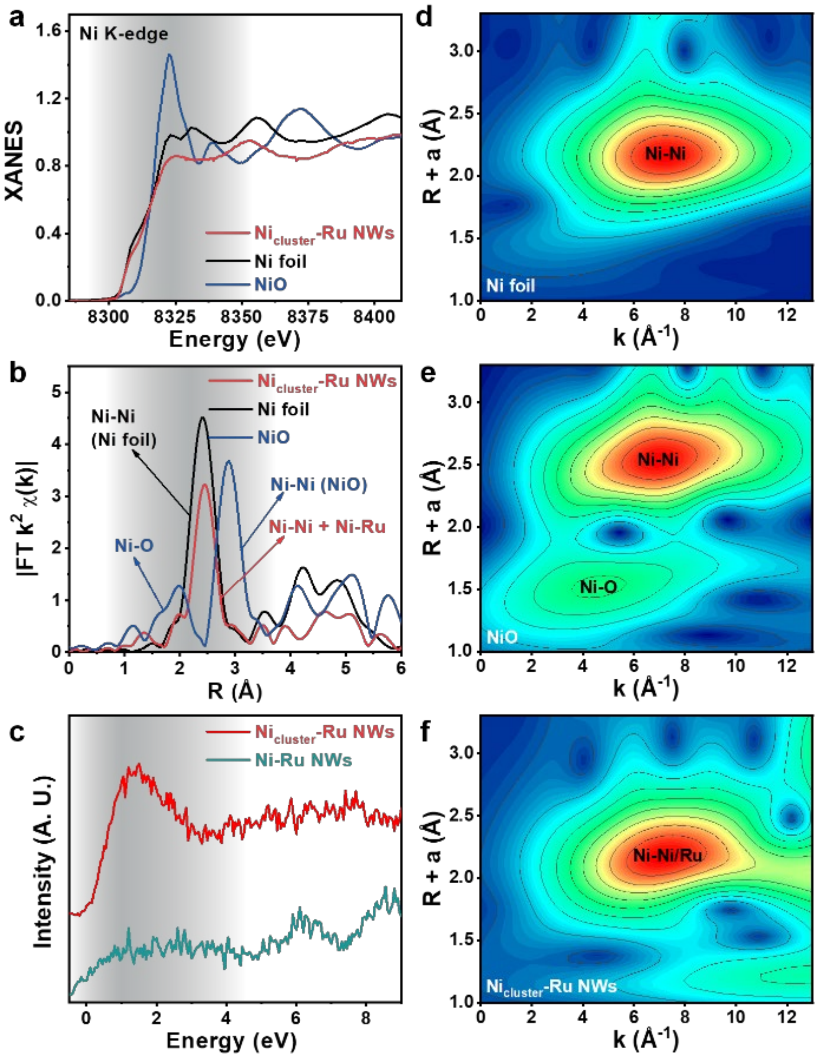

Fig. 3 EXAFS and XPS spectra of Ni$_{cluster}$-Ru NWs. (a) XANES and (b) Fourier transforms of EXAFS spectra of Ni$_{cluster}$-Ru NWs, NiO and Ni foil for the Ni K-edge. (c) Valence photoemission spectra of Ni$_{cluster}$-Ru NWs and Ni-Ru NWs. (d-f) Wavelet transforms for the k^2-weighted EXAFS signals of Ni foil, NiO and Ni$_{cluster}$-Ru NWs.

X-ray absorption near-edge structure (XANES) and the extended X-ray absorption fine structure (EXAFS) were used to study the charge states and crystal structure of Ni in Ni$_{cluster}$-Ru NWs.[19-22] The NiO and Ni foil were measured as references. The normalized Ni-K XANES in **Fig. 3a** shows that the Ni in Ni$_{cluster}$-Ru NWs is much similar to that of metallic Ni foil, but very different from that of NiO, suggesting a metallic state of Ni of our Ni$_{cluster}$-Ru NWs. In addition, the Fourier transform of Ni-K EXAFS (FT-EXAFS) spectrum in **Fig. 3b** reveals that the Ni$_{cluster}$-Ru NWs exhibits a peak located at 2.49 Å, slightly larger than the peak of Ni foil at around 2.48 Å. This can be attributed to the partial formation of the Ni-Ru coordination structure.[23]

Moreover, we can hardly observe a peak of Ni-O coordination around 2.07 Å, indicating again that the Ni in $Ni_{cluster}$-Ru NWs is in the metallic state, which is well reproduced through a fitting using Ni-Ni/Ru path (**Fig. S4 & Table S1**).[15, 24] It is worth mentioning that the Ni-Ni/Ru coordination number in $Ni_{cluster}$-Ru NWs is small, indicating the existence of small Ni species. We further used the wavelet transforms (WT) of the Ni K-edge EXAFS to examine the coordination features of $Ni_{cluster}$-Ru NWs. As shown in **Fig. 3d-f**, the WT contour plot of $Ni_{cluster}$-Ru NWs mainly exhibits one intensity maximum at approximately 7.25 $Å^{-1}$, which is ascribed to the Ni-Ni/Ni-Ru compared to those of NiO (6.95 $Å^{-1}$) and Ni foil (7.10 $Å^{-1}$).[25] All the above results confirm that Ni exists as Ni cluster in $Ni_{cluster}$-Ru NWs, being consistent with the result of STEM images.

We also used X-ray photoelectron spectroscopy (XPS) to explore the impact of Ni cluster on the surface chemical states of $Ni_{cluster}$-Ru NWs (**Fig. S5**). For $Ni_{cluster}$-Ru NWs, the peaks at 488.26 eV and 466.25 eV attributed to Ru^{4+} $3p_{1/2}$ and Ru^{4+} $3p_{3/2}$, and other peaks at 485.15 eV and 462.92 eV to Ru^0 $3p_{1/2}$ and Ru^0 $3p_{3/2}$, respectively.[26, 27] All Ru 3p peaks in $Ni_{cluster}$-Ru NWs negatively shifted by 0.2 eV compared to Ru NWs. This could be interpreted that by the introduction of Ni the local electronic structure of Ru is effectively changed.[24] We further use the valence photoemission spectra to reveal the electronic structure of $Ni_{cluster}$-Ru NWs, where the *d*-band states of Ni in $Ni_{cluster}$-Ru NWs becomes much sharper and narrower than that in Ni-Ru NWs, matching well with the simulation results (**Fig. 3c**). All these results suggest the successful synthesis of diluted Ni clusters decorated Ru NWs.

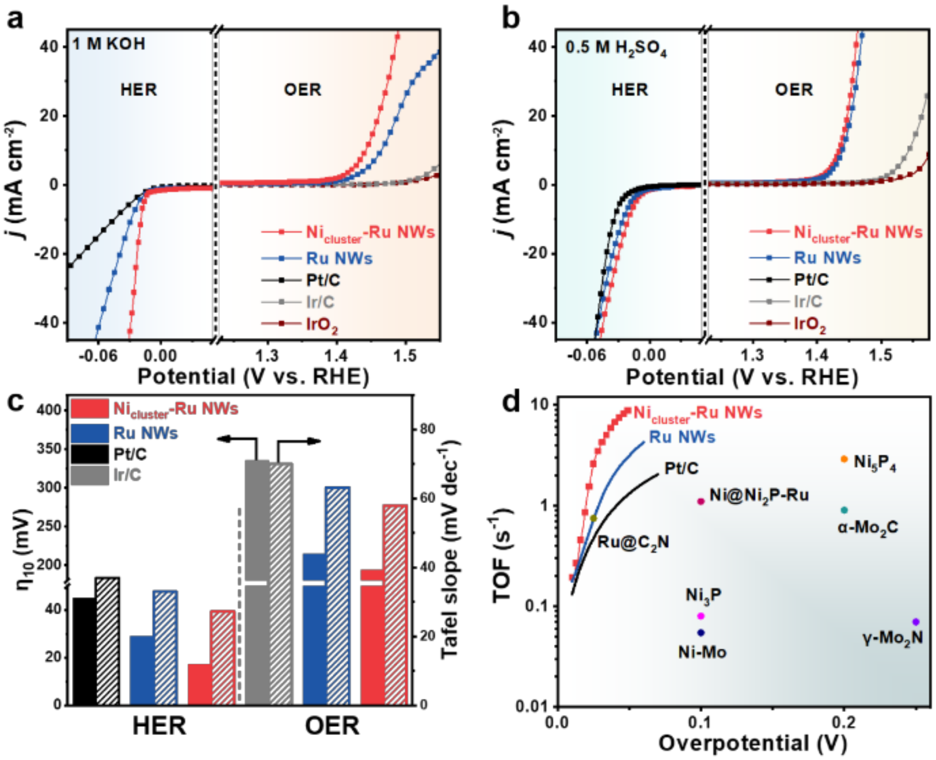

Fig. 4 HER and OER performances of $Ni_{cluster}$-Ru NWs under different pH conditions. HER and OER polarization curves of $Ni_{cluster}$-Ru NWs, Ru NWs, Pt/C, Ir/C and IrO_2 in (a) 1 M KOH and (b) 0.5 M H_2SO_4. (c) Overpotentials at 10 mA cm^{-2} and Tafel plots of $Ni_{cluster}$-Ru NWs, Ru NWs, Pt/C and Ir/C in 1 M KOH. (d) TOF values of HER of $Ni_{cluster}$-Ru NWs, Ru NWs, Pt/C and previously reported catalysts in 1 M KOH.

To reveal the facilitation of catalytic reaction due to diluted nanoclusters decorated nanowires, we first measured the HER performance of different electrocatalysts in 1 M KOH condition. The thermogravimetric analysis (TGA) curves indicated that the mass loading of Ru in the catalysts was nearly 20 wt% (**Fig. S2b-c**). As shown in **Fig. 4a**, $Ni_{cluster}$-Ru NWs exhibited the smallest overpotential of 17 mV at 10 mA cm^{-2}, which was better than those of Ru NWs (29 mV) and the commercial Pt/C (45 mV).[28] The Tafel slope was estimated to be 27 mV dec^{-1} for $Ni_{cluster}$-Ru NWs, lower than those of Ru NWs (33 mV dec^{-1}) and the commercial Pt/C (37 mV dec^{-1}), indicating the more efficient kinetics of $Ni_{cluster}$-Ru NWs towards HER (**Fig. 4c & S6**). Electrochemical impedance spectroscopy (EIS) was also performed to investigate the charge-transfer kinetics (**Fig. S7**),[29] where the $Ni_{cluster}$-Ru NWs exhibited the smallest charge-transfer resistance (R_{ct}) of 5.2 Ω, indicating the fast interfacial charge-transfer kinetics of HER, while the R_{ct} values of Ru NWs was recorded to be 9.3 Ω. Meanwhile, the calculated double-layer capacitance (C_{dl}) value from cyclic voltammogram (CV) curves revealed the electrochemical active surface areas (ECSAs) of different catalysts (**Fig. S8**).[30] We can see that the C_{dl} value of $Ni_{cluster}$-Ru NWs was calculated as 22.4 mF cm^{-2}, larger than Ru NWs (12.1 mF cm^{-2}), indicating that $Ni_{cluster}$-Ru NWs can provide more active sites for electrocatalysis.

To reveal the intrinsic activities of various electrocatalysts, the number of active sites and turnover frequencies (TOF) values were determined based on the underpotential deposition of copper (Cu-UPD) (**Fig. S9**). As observed in **Fig. 4d & Table S2**, the TOF values of $Ni_{cluster}$-Ru NWs at the overpotentials of 25 mV and 50 mV were 2.61 H_2 s^{-1} and 8.95 H_2 s^{-1}, respectively. Both values were larger than those of Ru NWs (0.72 H_2 s^{-1} at 25 mV and 3.13 H_2 s^{-1} at 50 mV), and the commercial Pt/C (0.47 H_2 s^{-1} at 25 mV and 1.32 H_2 s^{-1} at 50 mV). In addition, the high TOF value of $Ni_{cluster}$-Ru NWs was even superior to those of the recently reported electrocatalysts, such as Ru@C_2N (0.75 H_2 s^{-1} at 25 mV), Ni_3P (0.08 H_2 s^{-1} at 100 mV), Ni@Ni_2P-Ru (1.1 H_2 s^{-1} at 100 mV), Ni-Mo (0.05 H_2 s^{-1} at 100 mV), Ni_5P_4 (2.9 H_2 s^{-1} at 200 mV), α-Mo_2C (0.9 H_2 s^{-1} at 200 mV), ɣ-Mo_2N (0.07 H_2 s^{-1} at 250 mV),[27, 31-34] revealing the outstanding intrinsic HER activity of $Ni_{cluster}$-Ru NWs

Given the high catalytic performance of HER, the OER performance of $Ni_{cluster}$-Ru NWs in 1 M KOH was also evaluated. The commercial Ir/C was chosen for comparison. As shown in **Fig. 4a**, $Ni_{cluster}$-Ru NWs exhibited the best OER activity with the lowest overpotential of 194 mV at 10 mA cm^{-2}, lower than those of Ru NWs (215 mV), the commercial Ir/C (336 mV) and IrO_2 (370 mV). $Ni_{cluster}$-Ru NWs also presented the smallest Tafel slope of 58 mV dec^{-1}, better than Ru NWs (64 mV dec^{-1}) and the commercial Ir/C (70 mV dec^{-1}) (**Fig. S5**). The lower Tafel slope suggests the faster kinetics of OER, indicating the superior OER activity of $Ni_{cluster}$-Ru NWs.[35] As shown in **Fig. S10 & Table S3**, compared the OER performance with other reported catalysts in 1 M KOH, $Ni_{cluster}$-Ru NWs further show the best performance, which requires the lowest overpotential to achieve 10 mA cm^{-2}, demonstrating the highly efficient electrocatalysts of $Ni_{cluster}$-Ru NWs. Furthermore, we evaluated the mass activities of different catalysts by normalizing the mass of Ru (mass activity). As shown in **Fig. S11**, the mass activities are 1417 A g_{Ru}^{-1} and 461 A g_{Ru}^{-1} at the overpotential of 50 mV of $Ni_{cluster}$-Ru NWs and Ru NWs for HER, respectively, and 521 A g_{Ru}^{-1} and 246 A g_{Ru}^{-1} at the overpotential of 250 mV of $Ni_{cluster}$-Ru NWs and Ru NWs for OER, respectively.

The promising HER and OER activities of $Ni_{cluster}$-Ru NWs in 1 M KOH encouraged further evaluation in acidic condition (0.5 M H_2SO_4). As shown in **Fig. 4b & S10**, $Ni_{cluster}$-Ru NWs showed the best activity towards HER and OER in the acidic condition. $Ni_{cluster}$-Ru NWs requires a low overpotential to obtain 10 mA cm^{-2}, with 20 mV for HER and 205 mV for OER, much better than that of Ru NWs. Compared with the reported catalysts in 0.5 M H_2SO_4 (**Fig. S12 & Table S3**), $Ni_{cluster}$-Ru NWs have been demonstrated excellent performance for both HER and OER under the acidic condition.[31, 36-40] Furthermore, we also studied the performance of $Ni_{cluster}$-Ru NWs in 0.1 M KOH and 0.05 M H_2SO_4. Remarkably, it also exhibits excellent performance, where $Ni_{cluster}$-Ru NWs require the lowest overpotential in both HER (19 mV in 0.1 M KOH; 26 mV in 0.05 M H_2SO_4) and OER (210 mV in 0.1 M KOH; 207 mV in 0.05 M H_2SO_4) to reach a current density of 10 mA cm^{-2} (**Fig. S13-14**).[7] All the above results demonstrate that the superior activity of $Ni_{cluster}$-Ru NWs for HER and OER in both acidic and alkaline electrolytes.

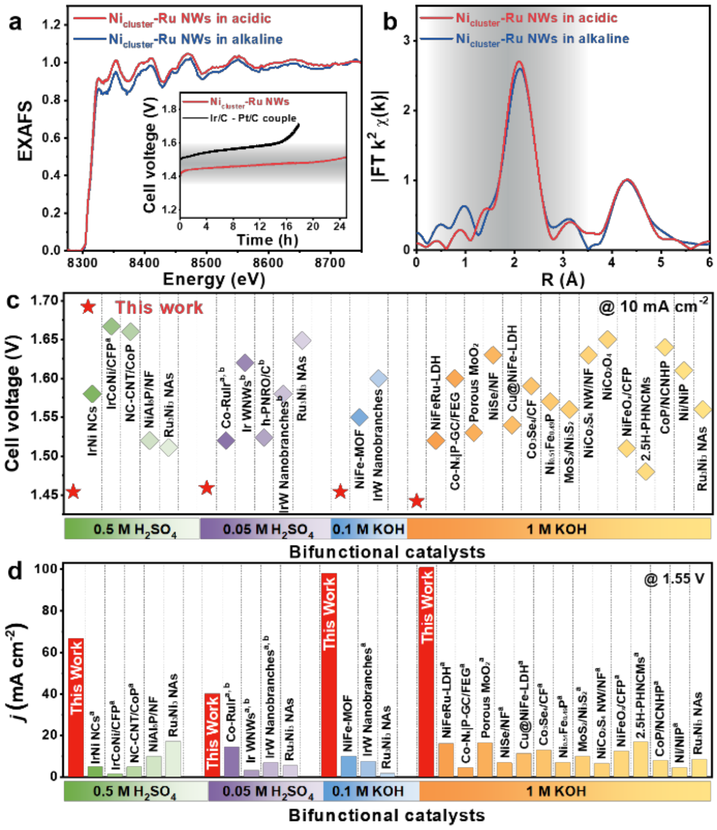

Fig. 5 Overall water splitting performances under different pH condition. (a) XANES spectra of $Ni_{cluster}$-Ru NWs after stability tests in different pH electrolytes. (insert: chronopotentiometry curves of $Ni_{cluster}$-Ru NWs and Ir/C-Pt/C couple in 1 M KOH at 5 mA cm^{-2}.) and (b) Fourier transforms of EXAFS spectra of $Ni_{cluster}$-Ru NWs after stability tests in different pH electrolytes. (c) Comparison of the cell voltages to achieve the current density of 10 mA cm^{-2} for $Ni_{cluster}$-Ru NWs with reported bifunctional catalysts under different pH conditions. (d) Comparison of the current densities at 1.55 V for $Ni_{cluster}$-Ru NWs with reported bifunctional catalysts under different pH conditions ([a]derived from estimates of data, [b]measured in 0.1 M $HClO_4$).

Inspired by the highly active HER and OER performance in different pH conditions, we further investigated the $Ni_{cluster}$-Ru NWs as the bifunctional catalyst in a two-electrode configuration for overall water splitting (**Fig. S15-16**). To reach the current density of 10 mA cm^{-2}, $Ni_{cluster}$-Ru NWs only require cell voltages of 1.454 V, 1.449 V, 1.454 V and 1.442 V in four pH values (0.5 M H_2SO_4, 0.05 M H_2SO_4, 0.1 M KOH and 1 M KOH), all which are lower than 1.50 V (**Fig. S17**). The electrical-to-fuel efficiencies of overall water splitting are as high as 84.59%, 84.89%, 84.59%, 85.30%, respectively. These values are also much lower than those of Ru NWs, Ir/C-Pt/C couple, IrO_2-Pt/C couple and many other available catalysts (**Fig. 5c & Table S4**). In addition, at 1.55 V cell voltage, we found that all the reported catalysts deliver the current density below 20 mA cm^{-2}. For a sharp contrast, $Ni_{cluster}$-Ru NWs can readily reach the current density of 40 mA cm^{-2}, even up to 100 mA cm^{-2} (1 M KOH), with applying only 1.55 V (**Fig. 5d**). Moreover, Ru-Ni NWs also exhibit a high performance than Ir/C-Pt/C couple and IrO_2-Pt/C couple, even in 0.1 M PBS solution (**Fig. S18**). The stability of $Ni_{cluster}$-Ru NWs was then evaluated by chronopotentiometry (**Fig. 5a**, inset and **Fig. S19-20**), where the $Ni_{cluster}$-Ru NWs shows almost negligible performance degradation during the stability test in both acid and alkaline elecrolytes. For comparison, the Ir/C-Pt/C couple exhibited an obvious decrease in less than 8 h. After the stability test, no obvious changes in morphology and composition of $Ni_{cluster}$-Ru NWs were observed, as confirmed by the TEM image and XPS spectra (**Fig. S21**). We further evaluated the detailed structure of $Ni_{cluster}$-Ru NWs after the long-term tests. As we observed in **Fig. S3** and **Fig. S22**. The acid solution can efficiently remove the Ni species on the surface of nanowires. Especially, after the HER and OER tests, the Ni contents of the catalyst did not decrease significantly (**Fig. S23 & Table S5-6**), which is consistent with the results of XPS (**Fig. S24**). These evidences indicate the effective and strong stabilization of diluted Ni nanoclusters on Ru nanowires, even after long-term stability tests. **Fig. 5a-b** show the EXAFS and the corresponding Fourier transform of EXAFS (FT-EXAFS) spectra of $Ni_{cluster}$-Ru NWs after stability tests in different pH conditions (1 M KOH and 0.5 M H_2SO_4). The similar coordination structure to that of the previous $Ni_{cluster}$-Ru NWs was observed, indicating the Ni nanoclusters can be strongly anchored on the surface of Ru NWs. All these results demonstrate the excellent structure stability of $Ni_{cluster}$-Ru NWs.

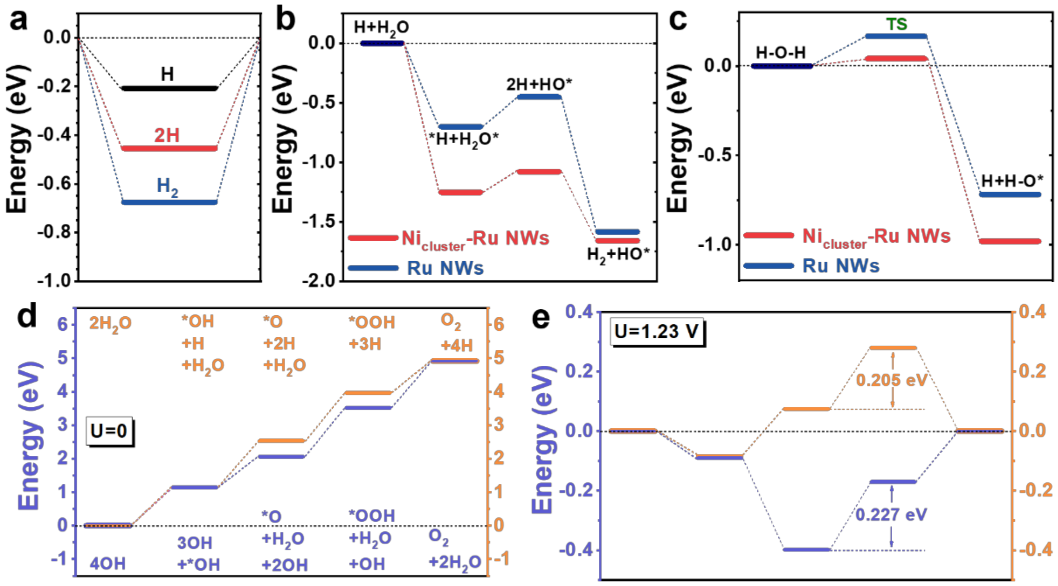

Fig. 6 Theoretically interpreted energetic activities for HER and OER. (a) H-adsorption energy of H, 2H, and H_2 on the $Ni_{cluster}$-Ru NWs. (b) Alkaline HER pathways for pristine Ru NWs and $Ni_{cluster}$-Ru NWs. (c) H_2O-splitting transition state barrier comparison. (d) The pathways of both four-electron based acidic and alkaline OER at U = 0 V. (e) The OER pathways are summarized at U = 1.23 V. The orange line indicates the reaction step in the acidic environment while the purple line indicates the reaction step in the alkaline environment.

We carried out DFT calculation to explore the energetic properties and pathways of both HER and OER on the pristine Ru NWs and $Ni_{cluster}$-Ru NWs. With the introduction of the Ni clusters on the surface, the initial H adsorption is energetically preferred with -0.20 eV gained. The subsequent 2H and the final formation of H_2 show a downhill energetic trend, guaranteeing the efficient HER process (**Fig. 6a**). For the HER in the alkaline environment, the more favourable reaction trend has been noted for $Ni_{cluster}$-Ru NWs. Especially for the initial H_2O, the $Ni_{cluster}$-Ru NWs display much more favoured adsorption than the pristine Ru, leading to the larger energy release and alleviated energy barrier (**Fig. 6b**). The transition-state comparison of H_2O splitting also proves the stronger capability of H-O-H bond cleavage on the $Ni_{cluster}$-Ru NWs, which potentially directs and promotes the H_2O splitting (**Fig. 6c**). Under such a strong water dissociation trend, the OER performances under both the alkaline and the acidic environments should also be beneficial. Under U = 0 V, the alkaline and acidic OER trends show a similar upward trend. However, for the transition of *OH towards O*, the alkaline environment shows a smaller barrier. Both acidic and the alkaline OER on $Ni_{cluster}$-Ru NWs indicate a larger energy barrier in the transition of O* to *OOH (**Fig. 6d**). With the applied potential of 1.23 V, the rate-determining step of OER in the alkaline and acidic has been identified as the formation of *OOH. In the acidic media, the OER shows a 0.205 eV barrier while the alkaline environment displays a slightly larger energy barrier of 0.227 eV (**Fig. 6e**). Therefore, the strong interactions between different Ru NWs and Ni cluster lead to the prominent overall H_2O-splitting performance in both the alkaline and acidic environment. We have also investigated the electronic structures and reaction trend of varied Ni cluster size on Ru NWs (**Fig. S25**), which further verified the superior performances of $Ni_{cluster}$-Ru NWs in this work. All these results conclude that the strong interaction between Ru and Ni nanocluster largely facilities the overall water splitting in the pH-universal conditions.

Conclusions

In summary, we have proposed a diluted metal nanoclusters-activated strategy for developing high-efficiency pH-universal water splitting electrocatalysts. Guided by theoretical calculation, the diluted Ni cluster activated Ru NWs catalyst was fabricated, which exhibited superior overall water splitting performances with all the cell voltages lower than 1.454 V at 10 mA cm^{-2} in a wide pH range from 0 to 14, much better than those of the commercial Pt/C and Ir/C. The Ru-4*d* bands impose the isolation effect on the Ni-3*d* bands to realize the *d*-band narrowing results, which pins the Ni-3*d* bands with preserved high electroactivity. This boosts up the electron transfer to guarantee the water-splitting efficiency in wide pH environments. The strong interaction between Ni nanocluster and Ru surface also contribute to excellent stability. This work paves out a new approach for realizing high-efficiency catalytic system for electrocatalysis and beyond.

Conflicts of interest

There are no conflicts to declare.

Acknowledgements

This work was financially supported by the Ministry of Science and Technology of China (2017YFA0208200, 2016YFA0204100), the National Natural Science Foundation of China (21571135, 21905188, 21771156), Young Thousand Talented Program, Jiangsu Province Natural Science Fund for Distinguished Young Scholars (BK20170003), China Postdoctoral Science Foundation Grant (2019M651937), Guangdong Provincial Key Laboratory of Energy Materials for Electric Power (No. 2018B030322001), the project of scientific and technologic infrastructure of Suzhou (SZS201708), the Priority Academic Program Development of Jiangsu Higher Education Institutions (PAPD), and the start-up supports from Soochow University. We acknowledge support from the Max Planck-POSTECH-Hsinchu Center for Complex Phase Materials. T.Z., S.L. and Bin. Huang are equally contributed.

References

1 Z. W. Seh, J. Kibsgaard, C. F. Dickens, I. Chorkendorff, J. K. Norskov and T. F. Jaramillo, Combining theory and experiment in electrocatalysis: Insights into materials design. *Science* **2017***, 355,* eaad4998.

2 B. Y. Xia, Y. Yan, N. Li, H. B. Wu, X. W. Lou and X. Wang, A metal-organic framework-derived bifunctional oxygen electrocatalyst. *Nat. Energy* **2016***, 1*, 15006.

3 M. Shao, Q. Chang, J. P. Dodelet and R. Chenitz, Recent advances in electrocatalysts for oxygen reduction reaction. *Chem. Rev.* **2016***, 116*, 3594-3657.

4 X. Zou and Y. Zhang, Noble metal-free hydrogen evolution catalysts for water splitting. *Chem. Soc. Rev.* **2015***, 44*, 5148-5180.

5 Y. Jiao, Y. Zheng, K. Davey and S.-Z. Qiao, Activity origin and catalyst design principles for electrocatalytic hydrogen evolution on heteroatom-doped graphene. *Nat. Energy* **2016***, 1*, 16130.

6 L. Z. Zhang, Y. Jia, G. P. Gao, X. C. Yan, N. Chen, J. Chen, M. T. Soo, B. Wood, D. J. Yang, A. J. Du and X. D. Yao, Graphene defects trap atomic Ni species for hydrogen and oxygen evolution reactions. *Chem* **2018***, 4*, 285-297.

7 Y. Jia, L. Zhang, G. Gao, H. Chen, B. Wang, J. Zhou, M. T. Soo, M. Hong, X. Yan, G. Qian, J. Zou, A. Du and X. Yao, A heterostructure coupling of exfoliated Ni-Fe hydroxide nanosheet and defective graphene as a bifunctional electrocatalyst for overall water splitting. *Adv. Mater.* **2017***, 29*, 1700017.

8 T. R. Cook, D. K. Dogutan, S. Y. Reece, Y. Surendranath, T. S. Teets and D. G. Nocera, Solar energy supply and storage for the legacy and nonlegacy worlds. *Chem. Rev.* **2010***, 110*, 6474-6502.

9 T. Zheng, C. Shang, Z. He, X. Wang, C. Cao, H. Li, R. Si, B. Pan, S. Zhou and J. Zeng, Intercalated iridium diselenide electrocatalysts for efficient pH-universal water splitting. *Angew. Chem. Int. Ed.* **2019***, 58*, 14764-14769.

10 B. You, M. T. Tang, C. Tsai, F. Abild-Pedersen, X. Zheng and H. Li, Enhancing electrocatalytic water splitting by strain engineering. *Adv. Mater.* **2019***, 31*, e1807001.

11 Q. Yao, B. Huang, N. Zhang, M. Sun, Q. Shao and X. Huang, Channel-rich RuCu nanosheets for pH-universal overall water splitting electrocatalysis. *Angew. Chem. Int. Ed.* **2019***, 58*, 13983-13988.

12 G. Chen, C. Xu, X. Huang, J. Ye, L. Gu, G. Li, Z. Tang, B. Wu, H. Yang, Z. Zhao, Z. Zhou, G. Fu and N. Zheng, Interfacial electronic effects control the reaction selectivity of platinum catalysts. *Nat. Mater.* **2016***, 15*, 564-569.

13 F. Studt, F. Abild-Pedersen, T. Bligaard, R. Z. Sorensen, C. H. Christensen and J. K. Norskov, Identification of non-precious metal alloy catalysts for selective hydrogenation of acetylene. *Science* **2008***, 320*, 1320-1322.

14 Z. J. Zhao, S. H. Liu, S. J. Zha, D. F. Cheng, F. Studt, G. Henkelman and J. L. Gong, Theory-guided design of catalytic materials using scaling relationships and reactivity descriptors. *Nat. Rev. Mater.* **2019***, 4*, 792-804.

15 M. F. Li, K. N. Duanmu, C. Z. Wan, T. Cheng, L. Zhang, S. Dai, W. X. Chen, Z. P. Zhao, P. Li, H. L. Fei, Y. M. Zhu, R. Yu, J. Luo, K. T. Zang, Z. Y. Lin, M. N. Ding, J. Huang, H. T. Sun, J. H. Guo, X. Q. Pan, W. A. Goddard, P. Sautet, Y. Huang and X. F. Duan, Single-atom tailoring of platinum nanocatalysts for high-performance multifunctional electrocatalysis. *Nat. Catal.* **2019***, 2*, 495-503.

16 M. T. Greiner, T. E. Jones, S. Beeg, L. Zwiener, M. Scherzer, F. Girgsdies, S. Piccinin, M. Armbruster, A. Knop-Gericke and R. Schlogl, Free-atom-like *d* states in single-atom alloy catalysts. *Nat. Chem.* **2018***, 10*, 1008-1015.

17 S. Q. Zhu, Q. Wang, X. P. Qin, M. Gu, R. Tao, B. P. Lee, L. L. Zhang, Y. Z. Yao, T. H. Li and M. H. Shao, Tuning structural and compositional effects in Pd-Au nanowires for highly selective and active CO_2 electrochemical reduction reaction. *Adv. Energy Mater.* **2018***, 8*, 1802238.

18 N. Cheng, S. Stambula, D. Wang, M. N. Banis, J. Liu, A. Riese, B. Xiao, R. Li, T. K. Sham, L. M. Liu, G. A. Botton and X. Sun, Platinum single-atom and cluster catalysis of the hydrogen evolution reaction. *Nat. Commun.* **2016***, 7*, 13638.

19 J. Yang, L. Zhou, J. Cheng, Z. Hu, C. Kuo, C. W. Pao, L. Jang, J. F. Lee, J. Dai, S. Zhang, S. Feng, P. Kong, Z. Yuan, J. Yuan, Y. Uwatoko, T. Liu, C. Jin and Y. Long, Charge transfer induced multifunctional transitions with sensitive pressure manipulation in a metal-organic framework. *Inorg Chem* **2015***, 54*, 6433-6438.

20 Z. Liu, Y. Sakai, J. Yang, W. Li, Y. Liu, X. Ye, S. Qin, J. Chen, S. Agrestini, K. Chen, S. C. Liao, S. C. Haw, F. Baudelet, H. Ishii, T. Nishikubo, H. Ishizaki, T. Yamamoto, Z. Pan, M. Fukuda, K. Ohashi, K. Matsuno, A. Machida, T. Watanuki, S. I. Kawaguchi, A. M. Arevalo-Lopez, C. Jin, Z. Hu, J. P. Attfield, M. Azuma and Y. Long, Sequential spin state transition and intermetallic charge transfer in $PbCoO_3$. *J. Am. Chem. Soc.* **2020***, 142*, 5731-5741.

21 H. Liu, J. Zhou, L. Zhang, Z. Hu, C. Kuo, J. Li, Y. Wang, L. H. Tjeng, T.-W. Pi, A. Tanaka, L. Song, J.-Q. Wang and S. Zhang, Insight into the role of metal-oxygen bond and O 2p hole in high-voltage cathode $LiNi_xMn_{2-x}O_4$. *J. Phys. Chem. C* **2017***, 121*, 16079-16087.

22 S. Song, J. Zhou, S. Zhang, L. Zhang, J. Li, Y. Wang, L. Han, Y. Long, Z. Hu and J.-Q. Wang, Molten-salt synthesis of porous $La_{0.6}Sr_{0.4}Co_{0.2}Fe_{0.8}O_{2.9}$ perovskite as an efficient electrocatalyst for oxygen evolution. *Nano Research* **2018***, 11*, 4796-4805.

23 J. Mao, C. T. He, J. Pei, W. Chen, D. He, Y. He, Z. Zhuang, C. Chen, Q. Peng, D. Wang and Y. Li, Accelerating water dissociation kinetics by isolating cobalt atoms into ruthenium lattice. *Nat. Commun.* **2018***, 9*, 4958.

24 Z. Zhang, G. Liu, X. Cui, B. Chen, Y. Zhu, Y. Gong, F. Saleem, S. Xi, Y. Du, A. Borgna, Z. Lai, Q. Zhang, B. Li, Y. Zong, Y. Han, L. Gu and H. Zhang, Crystal phase and architecture engineering of lotus-thalamus-shaped Pt-Ni anisotropic superstructures for highly efficient electrochemical hydrogen evolution. *Adv. Mater.* **2018***, 30*, e1801741.

25 Y. Y. Zhou, Z. Y. Xie, J. X. Jiang, J. Wang, X. Y. Song, Q. He, W. Ding and Z. D. Wei, Lattice-confined Ru clusters with high CO tolerance and activity for the hydrogen oxidation reaction. *Nat. Catal.* **2020***, 3*, 454-462.

26 J. Su, R. Ge, K. Jiang, Y. Dong, F. Hao, Z. Tian, G. Chen and L. Chen, Assembling ultrasmall copper-doped ruthenium oxide nanocrystals into hollow porous polyhedra: highly robust electrocatalysts for oxygen evolution in acidic media. *Adv. Mater.* **2018**, *30*, e1801351.

27 Y. Liu, S. Liu, Y. Wang, Q. Zhang, L. Gu, S. Zhao, D. Xu, Y. Li, J. Bao and Z. Dai, Ru modulation effects in the synthesis of unique rod-like Ni@Ni_2P-Ru heterostructures and their remarkable electrocatalytic hydrogen evolution performance. *J. Am. Chem. Soc.* **2018***, 140*, 2731-2734.

28 J. Su, Y. Yang, G. Xia, J. Chen, P. Jiang and Q. Chen, Ruthenium-cobalt nanoalloys encapsulated in nitrogen-doped graphene as active electrocatalysts for producing hydrogen in alkaline media. *Nat. Commun.* **2017***, 8*, 14969.

29 Y. Shi, Y. Zhou, D. R. Yang, W. X. Xu, C. Wang, F. B. Wang, J. J. Xu, X. H. Xia and H. Y. Chen, Energy level engineering of MoS_2 by transition-metal doping for accelerating hydrogen evolution reaction. *J. Am. Chem. Soc.* **2017***, 139*, 15479-15485.

30 G. Chen, T. Wang, J. Zhang, P. Liu, H. Sun, X. Zhuang, M. Chen and X. Feng, Accelerated hydrogen evolution kinetics on NiFe-layered double hydroxide electrocatalysts by tailoring water dissociation active sites. *Adv. Mater.* **2018***, 30*, 1706279.

31 J. Mahmood, F. Li, S. M. Jung, M. S. Okyay, I. Ahmad, S. J. Kim, N. Park, H. Y. Jeong and J. B. Baek, An efficient and pH-universal ruthenium-based catalyst for the hydrogen evolution reaction. *Nat. Nanotechnol.* **2017***, 12*, 441-446.

32 A. B. Laursen, K. R. Patraju, M. J. Whitaker, M. Retuerto, T. Sarkar, N. Yao, K. V. Ramanujachary, M. Greenblatt and G. C. Dismukes, Nanocrystalline Ni_5P_4: a hydrogen evolution electrocatalyst of exceptional efficiency in both alkaline and acidic media. *Energy Environ. Sci.* **2015***, 8*, 1027-1034.

33 J. R. McKone, B. F. Sadtler, C. A. Werlang, N. S. Lewis and H. B. Gray, Ni-Mo Nanopowders for Efficient Electrochemical Hydrogen Evolution. *ACS Catal.* **2013***, 3*, 166-169.

34 L. Ma, L. R. L. Ting, V. Molinari, C. Giordano and B. S. Yeo, Efficient hydrogen evolution reaction catalyzed by molybdenum carbide and molybdenum nitride nanocatalysts synthesized via the urea glass route. *J. Mater. Chem. A* **2015**, *3*, 8361-8368.

35 Z. Cai, Y. M. Bi, E. Y. Hu, W. Liu, N. Dwarica, Y. Tian, X. L. Li, Y. Kuang, Y. P. Li, X. Q. Yang, H. L. Wang and X. M. Sun, Single- Single-crystalline ultrathin Co_3O_4 nanosheets with massive vacancy defects for enhanced electrocatalysis. *Adv. Energy Mater.* **2018**, *8*, 1701694.

36 E. J. Popczun, J. R. McKone, C. G. Read, A. J. Biacchi, A. M. Wiltrout, N. S. Lewis and R. E. Schaak, Nanostructured nickel phosphide as an electrocatalyst for the hydrogen evolution reaction. *J. Am. Chem. Soc.* **2013**, *135*, 9267-9270.

37 T. F. Jaramillo, K. P. Jorgensen, J. Bonde, J. H. Nielsen, S. Horch and I. Chorkendorff, Identification of active edge sites for electrochemical H_2 evolution from MoS_2 nanocatalysts. *Science* **2007**, *317*, 100-102.

38 H. W. Liang, S. Bruller, R. Dong, J. Zhang, X. Feng and K. Mullen, Molecular metal-N_x centres in porous carbon for electrocatalytic hydrogen evolution. *Nat. Commun.* **2015**, *6*, 7992.

39 E. J. Popczun, C. G. Read, C. W. Roske, N. S. Lewis and R. E. Schaak, Highly active electrocatalysis of the hydrogen evolution reaction by cobalt phosphide nanoparticles. *Angew. Chem. Int. Ed.* **2014**, *53*, 5427-5430.

40 H. Fei, J. Dong, M. J. Arellano-Jimenez, G. Ye, N. Dong Kim, E. L. Samuel, Z. Peng, Z. Zhu, F. Qin, J. Bao, M. J. Yacaman, P. M. Ajayan, D. Chen and J. M. Tour, Atomic cobalt on nitrogen-doped graphene for hydrogen generation. *Nat. Commun.* **2015**, *6*, 8668.

TOC